


Separation of Heating and Magnetoelastic Coupling Effects in Surface-Acoustic-Wave-Enhanced Creep of Magnetic Domain Walls

Jintao Shuai¹, Robbie G. Hunt¹, Thomas A. Moore^{1,*}, and John E. Cunningham^{2,†}

¹*School of Physics and Astronomy, University of Leeds, Leeds, LS2 9JT, United Kingdom*

²*School of Electronic and Electrical Engineering, University of Leeds, Leeds, LS2 9JT, United Kingdom*

 (Received 1 March 2023; revised 21 April 2023; accepted 12 May 2023; published 5 July 2023)

Surface acoustic waves (SAWs) have significant potential for energy-efficient control of magnetic domain walls (DWs) owing to the magnetoelastic coupling effect. However, the dissipation of radio-frequency (rf) power in a SAW device can result in heating, which can also affect the DW motion. In this work, the heating of a SAW device consisting of a Pt/Co/Ta thin film with perpendicular magnetic anisotropy in between two interdigitated transducers is measured *in situ* with use of an on-chip Pt film as a thermometer within the SAW beam path. The application of SAWs at a center frequency of 48 MHz and a total rf power of 21 dBm results in a temperature increase of approximately 10 K within the SAW beam path owing to rf-power dissipation. DW velocity in a Pt/Co/Ta thin film is evaluated separately with use of Kerr microscopy at various temperatures or in the presence of SAWs. With a 10-K increase in temperature only, the DW velocity is found to increase from $33 \pm 3 \mu\text{m/s}$ (at room temperature) to $104 \pm 8 \mu\text{m/s}$ under an external magnetic field of 65 Oe. Traveling-SAW-assisted DW velocity ($116 \pm 3 \mu\text{m/s}$) is slightly higher than that with a 10-K temperature increase alone, suggesting that the heating plays the major role in promoting DW motion, whereas the DW motion is significantly enhanced ($418 \pm 8 \mu\text{m/s}$) in the presence of standing SAWs, indicating that magnetoelastic coupling is more important than heating in this scenario.

DOI: [10.1103/PhysRevApplied.20.014002](https://doi.org/10.1103/PhysRevApplied.20.014002)

I. INTRODUCTION

Magnetic domain wall (DW) motion in thin films with perpendicular magnetic anisotropy shows potential for technological applications in spintronics, such as magnetic racetrack memory and logic devices [1–7]. DW creep motion, which occurs below a critical field H_{dep} and at a finite temperature T , is the characteristic motion of a 1D elastic interface propagating through a 2D disordered medium. The velocity of DW creep motion can be described as [8–10]

$$v = v_0 \exp\left(-\frac{U_c}{k_B T} \left(\frac{H_{\text{dep}}}{H}\right)^{\frac{1}{4}}\right), \quad (1)$$

where U_c is the pinning energy barrier induced by the disordered energy landscape, H is the applied field, k_B

is the Boltzmann constant, and v_0 is a numerical prefactor [9,11]. Therefore, to enhance the DW creep motion, one can decrease the pinning energy barrier, increase the magnetic field, or increase the temperature.

Surface acoustic waves (SAWs) are acoustic waves traveling along the surface of a material exhibiting elasticity, which can introduce dynamic strain waves propagating distances of millimeters through magnetic thin films [12]. The magnetoelastic energy density may be expressed as

$$F_{\text{ME}} = B_1 \sum_{i=x,y,z} m_i^2 \epsilon_{ii} + B_2 \sum_{i \neq j} m_i m_j \epsilon_{ij}, \quad (2)$$

where B_1 and B_2 are the longitudinal and shear magnetoelastic coefficients, which are material dependent, and ϵ_{ij} is the strain tensor. Owing to the magnetoelastic coupling effect, dynamic strain waves create a dynamic energy landscape and therefore trigger the magnetization precession [13–15], assist the magnetization switching [16,17], and enhance the DW motion [18–22]. For example, Dean *et al.* [23] theoretically showed that multiple DWs could be moved synchronously by changing the frequency of standing SAWs. Edrington *et al.* [20] demonstrated that standing SAWs can be an effective driver of DW motion in Co/Pt multilayers. Adhikari *et al.* [18,24] investigated the

*t.a.moore@leeds.ac.uk

†j.e.cunningham@leeds.ac.uk

Published by the American Physical Society under the terms of the [Creative Commons Attribution 4.0 International](https://creativecommons.org/licenses/by/4.0/) license. Further distribution of this work must maintain attribution to the author(s) and the published article's title, journal citation, and DOI.

impact of SAWs on enhancing DW motion and increasing the likelihood of DW depinning.

The applied radio-frequency (rf) power and the propagation of SAWs through a structure can result in a global or local temperature increase in devices due to either the dissipation of the rf power or acoustothermal heating from the SAW [25–28]. These temperature increases can also contribute to the DW motion. The acoustothermal heating effect is often discussed in the context of the interaction of SAWs with microfluidic systems [26,29–35]. For example, Wang *et al.* [34] investigated SAWs as a rapid and controllable acoustothermal microheater for both the sessile droplet and liquid within a polydimethylsiloxane microchamber. Utko *et al.* [27], on the other hand, found that the rf-heating effect plays more important role than the SAW itself in a SAW-driven single-electron pump.

Evaluation of the different possible heating mechanisms in SAW-magnetic thin film system is therefore crucial to distinguish between heating and SAW-induced effects. To date, no systematic study on heating effects in such systems has been reported. In this study, we examine the heating of a SAW device that comprises a Pt/Co/Ta thin film with perpendicular magnetic anisotropy in the presence of standing or traveling SAWs within a frequency range of 46–51 MHz and at a power of 21 dBm. The heating is measured *in situ* with use of Pt thin film thermometers placed at several locations on the same chip, including within the SAW beam path. DW velocity is also separately determined at different temperatures, firstly with no SAW applied, and secondly in the presence of standing or traveling SAWs, allowing us to discuss and investigate fully the origin and impact of heating, and to distinguish it from the SAW-driven effects.

II. METHODS

Figure 1(a) shows a schematic of the SAW device. A 2-mm-wide Ta(5.0 nm)/Pt(2.5 nm)/Co(0.9 nm)/Ta(5.0 nm) [see Fig. 1(c)] thin film with perpendicular magnetic anisotropy is prepared at the center of an 128° Y-cut lithium niobate (LiNbO₃) substrate with dimensions of 10 × 12 × 0.5 mm³ by dc magnetron sputtering in a vacuum system with a base pressure of 3.0 × 10⁻⁶ Pa. A pair of Ti(10 nm)/Au(90 nm) interdigitated transducers (IDTs) are patterned at either end of the magnetic thin film by optical lithography followed by metal evaporation and liftoff. Each IDT consists of 20 pairs of electrodes. The aperture of the IDTs (length of the electrodes) and the SAW propagation distance (distance between the two IDTs) are 500 μm and 4.5 mm, respectively. The electrode width and pitch are both designed to be 20 μm, resulting in a SAW wavelength of approximately 80 μm. A Pt film with dimensions of 200 × 200 × 0.075 μm³ is used to determine the temperature changes; this is patterned by dc sputtering and is located in between the magnetic thin film and IDTs within

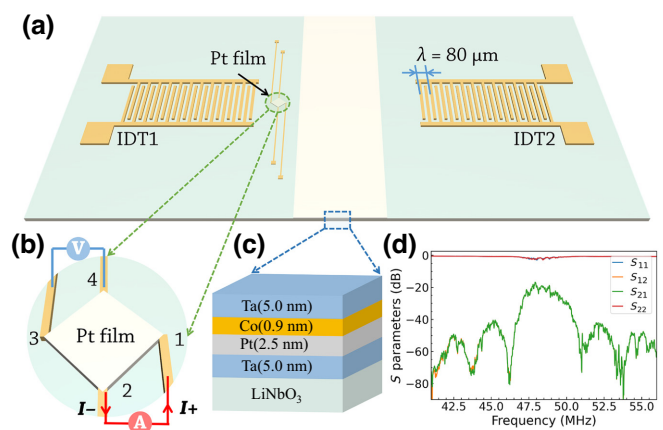


FIG. 1. (a) The SAW device (not to scale). A 2-mm-wide magnetic thin film is deposited by dc sputtering onto a lithium niobate (LiNbO₃) substrate. A pair of IDTs, which can be used to launch SAWs with a wavelength of 80 μm, are fabricated at opposite ends of the magnetic thin film. A Pt film is patterned in between the magnetic thin film and the IDTs and within the SAW beam path. (b) The electrical transport measurements using Pt film. Current passes through ports 1 and 2, while voltage is measured with use of ports 3 and 4 simultaneously. (c) Structure of the Ta(5.0 nm)/Pt(2.5 nm)/Co(0.9 nm)/Ta(5.0 nm) thin film. (d) S parameters for the IDTs used to launch SAWs. The delay line comprising both IDTs and the substrate shows a center frequency of 48 MHz.

the SAW beam path. The distance from the thermometer (within the SAW beam path) center to the thin film edge is 250 μm. Figure 1(b) shows a schematic of the Pt film. Four terminal electrical transport measurements are performed with use of a combined Keithley 6221-2182A current source [connected to ports 1 and 2 in Fig. 1(b)] and a nanovoltmeter [connected to ports 3 and 4 in Fig. 1(b)]. Scattering parameters (S parameters) are determined by a vector network analyzer (Agilent E5062A). Figure 1(d) shows the reflection (S_{11} and S_{22}) and transmission (S_{21} and S_{12}) characteristics of the SAW transducers and substrate exhibiting a center frequency of 48 MHz. Standing SAWs are generated by application of rf signals to both IDT1 and IDT2 simultaneously [see Fig. 1(a)], whereas rf signals applied to either IDT1 or IDT2 alone are used to launch traveling SAWs, referred to as “TW1” and “TW2”, respectively. Power loss along the circuit is carefully examined and compensated to ensure the total power sent to the IDTs is the same as that for sending SAWs and traveling SAWs. A description of the rf circuit used to determine S parameters and launch SAWs is given in Supplemental Material (Sec. I) [36].

The temperature change (ΔT) at the Pt thermometer is obtained by

$$\Delta T = \alpha(R - R_{RT}), \quad (3)$$

where α is the temperature change of the Pt per unit resistance (K/m Ω), R is the measured Pt resistance, and R_{RT} is the Pt resistance at room temperature. The resistance of Pt linearly increases with increasing temperature (see Fig S. 2a in the Supplemental Material), and α is 0.888 ± 0.004 K/m Ω as determined across a temperature range from 250 to 280 K. R_{RT} is measured at the beginning and the end of each measurement (see Fig S. 2b in the Supplemental Material). Further details of the temperature measurement are given in Supplemental Material (Sec. II) [36].

The DW velocity is determined by wide-field Kerr microscopy. The magnetic thin film is firstly saturated with a magnetic field of -300 Oe (coercivity of the thin film is approximately 60 Oe). Domains are nucleated with a short magnetic field pulse with opposite direction (50 Oe for 0.2 s). Another pulsed magnetic field is applied to move the DW. The gradient of the linear fitting of the DW propagating distances against different pulse widths is the DW velocity. The full method used to determine DW velocity is given in Supplemental Material (Sec. III) [36]. DW velocity is firstly measured from 19°C (room temperature) to 49°C ($\Delta T = 30$ K) without SAWs. The sample is heated by the hot side of a Peltier device placed underneath the sample. DW velocity is also measured in the presence of standing SAWs and then traveling SAWs at a frequency of 48 MHz and a power of 21 dBm with no heating applied from the Peltier device.

III. RESULTS AND DISCUSSION

Figures 2(a) and 2(b) show the temperature changes (ΔT) of the thermometer within the SAW beam path against source frequency with a total rf power of 21 dBm. We focus on the temperature changes within the SAW bandwidth [from 46 to 51 MHz, corresponding to the center peak in Fig. 1(d)]. In the presence of standing SAWs, four temperature peaks (approximately 47.38 MHz, approximately 48.00 MHz, approximately 48.85 MHz, and approximately 49.75 MHz) can be observed, with the largest ΔT of 10.4 ± 0.5 K at the center frequency of 48 MHz [SW in Fig. 2(a)]. The formation of the four resonance peaks can be explained by the constructive and destructive interference at certain frequencies causing different mechanical reflections at the IDTs.

On application of traveling SAWs [TW1 and TW2 in Fig. 2(a)], the temperature of the Pt increases as the center frequency is approached, reaching a maximum near the center frequency, with a few local minimum temperatures due to rf reflections from the IDT and sample edges. This trend roughly follows the reflection and transmission coefficients, which are overlaid on ΔT in Fig. 2(a). TW1 causes a slightly higher temperature increase at lower frequencies than TW2. For example, at 47 MHz, the temperature increases are 8.1 ± 0.2 K and 5.5 ± 0.3 K for

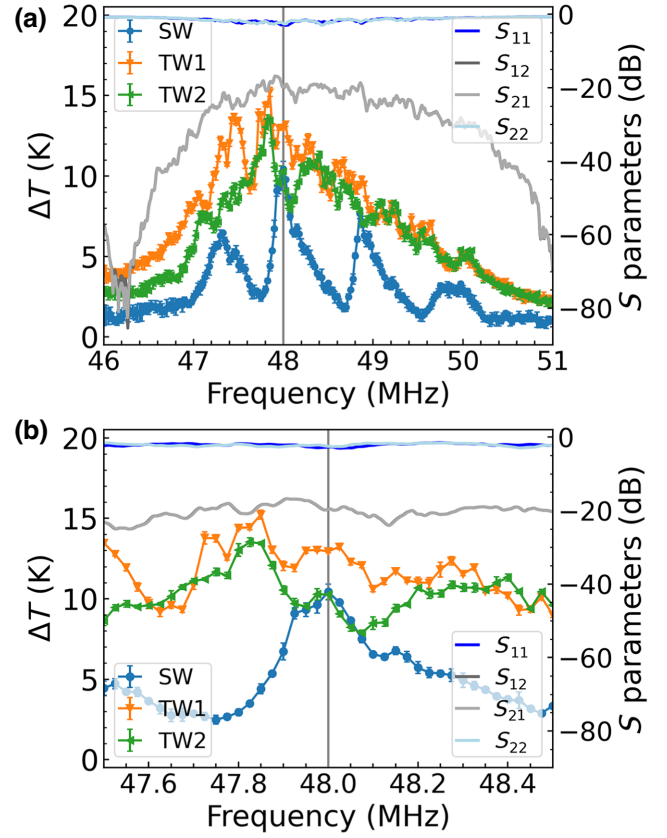


FIG. 2. (a) Temperature changes (ΔT) of the Pt within the SAW beam path as a function of source frequency from 46 to 51 MHz with rf power of 21 dBm. (b) Enlargement of temperature changes of the device against SAW frequencies from 47.5 to 48.5 MHz. SW, TW1, and TW2 denote standing SAWs, traveling SAWs launched from IDT1, and traveling SAWs launched from IDT2, respectively. The lines are a guide for the eye.

TW1 and TW2, respectively. This is due to this thermometer being closer to IDT1, implying dissipation of rf power at the transducer or its bonded wire is contributing to the observed change in temperature. The highest temperature increases for TW1 and TW2 occur at 47.85 and 47.83 MHz, respectively, with values of 15.2 ± 0.3 K and 13.5 ± 0.3 K, as listed in Table I.

TABLE I. Maximum temperature changes (ΔT_{\max}) of the device and corresponding frequencies, and temperature changes at the center frequency ($\Delta T_{48\text{ MHz}}$) in the presence of SAWs.

| SAW | ΔT_{\max} (K) | Corresponding frequency (MHz) | $\Delta T_{48\text{ MHz}}$ (K) |
|--------------|-----------------------|-------------------------------|--------------------------------|
| Standing SAW | 10.4 ± 0.5 | 48.00 | 10.4 ± 0.5 |
| TW1 | 15.2 ± 0.3 | 47.85 | 12.9 ± 0.1 |
| TW2 | 13.5 ± 0.3 | 47.83 | 10.3 ± 0.3 |

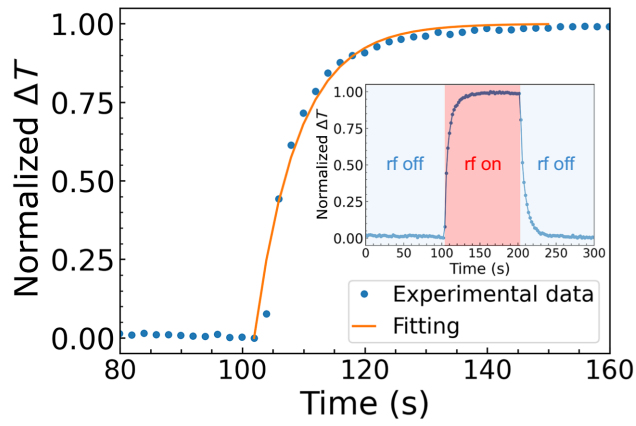


FIG. 3. Normalized temperature changes (ΔT) versus time (80–160 s) corresponding to the thermometer temperature increases from room temperature to equilibrium temperature in the presence of SAWs. The solid line in the main graph represents experimental data fit with Fourier’s law. The inset plot shows the normalized ΔT throughout the process: the temperature is continuously measured first without rf power (0–100 s), then with rf power applied (100–200 s), and finally 100 s after rf power is removed.

At 48 MHz, the temperature increases are 12.9 ± 0.1 K and 10.3 ± 0.3 K for TW1 and TW2, respectively, as shown in Fig. 2(b). Temperature changes of the thermometer within the SAW beam path in a wider frequency range can be found in Fig S.4 in Supplemental Material [36].

The source of heating in a SAW thin-film system could be either rf-power dissipation or the acoustothermal effect introduced by the SAW itself [25,28]. However, since IDTs operate with the highest efficiency at their resonant frequency (both rf-power dissipation and SAW amplitude depend strongly on the radio frequency), it is not possible to simply apply off-resonance rf signals to disentangle the two mechanisms. To distinguish between the two possible mechanisms, we investigate the thermal behavior of the thermometers. The temperature of the thermometer rapidly rises after the rf power is applied, and reaches a steady state after about 30 s, as shown in Fig. 3.

We propose a simple model of the observed heating as follows: Let T_s be the temperature of the source and T be the temperature of the thermometer. On the basis of Fourier’s law, the heat influx rate is estimated as

$$\dot{q}_{\text{in}}(t) = \frac{kA}{r}(T - T_s), \quad (4)$$

where r is the distance from the source of heating, A is the surface area of heat exchange, and k is thermal conductivity of the material. We denote $C_1 = kA/r$ to be the thermal conductance of the material. To account for heat loss, we assume that it occurs via conduction and convection, which

can be expressed as

$$\dot{q}_{\text{out}} = C_2(T - T_{\text{env}}), \quad (5)$$

where T_{env} is the temperature of the surroundings and C_2 is the corresponding thermal conductance. The equilibrium temperature T_{eq} can be expressed as

$$T_{\text{eq}} = \frac{C_1 T_s + C_2 T_{\text{env}}}{C_1 + C_2}. \quad (6)$$

Before the equilibrium is achieved we use

$$\dot{q}_t = \dot{q}_{\text{in}} - \dot{q}_{\text{out}}, \quad (7)$$

where \dot{q}_t is the heat absorbed by the thermometer. If c is the heat capacity of the thermometer, then Eq. (7) can be rewritten as

$$\dot{T} = \frac{C_1 + C_2}{c} (-T + T_{\text{eq}}). \quad (8)$$

Solving Eq. (8) gives the temperature change over time:

$$T = T_{\text{eq}} - (T_{\text{eq}} - T_0) \exp\left(-\frac{C_1 + C_2}{c}t\right). \quad (9)$$

From the experimental data, we fit T versus t to $T = T_{\text{eq}} - (T_{\text{eq}} - T_{\text{env}}) \exp(-\tilde{\gamma}t)$. The experimentally obtained $\tilde{\gamma}$ is expected to correspond to $(C_1 + C_2)/c$. Substituting $C_1 = k(A/r)$, we obtain

$$\tilde{\gamma} = \left(\frac{kA}{c}\right) \frac{1}{r} + \frac{C_2}{c}. \quad (10)$$

We choose to study the $\tilde{\gamma}$ value because it represents the “heating rate” and provides information about the entire heating process, enabling us to better understand its dynamics and variations at different locations. In contrast, temperature represents only the final result of the heating process and does not provide information about its dynamics.

Figure 4(a) shows a schematic layout of the SAW device. Temperature measurements are conducted both inside and outside the SAW beam path in the presence of the traveling SAW launched from IDT1. The rf power and frequency are set as 21 dBm and 48 MHz, respectively. The thermometer P0 in Fig. 4(a) is the same one as in Fig. 1(a), which is situated within the SAW beam path and is expected to experience the SAWs passing through. P1, P1’, P2, P2’, P3, and P3’ are thermometers that are situated outside the SAW beam path, where the SAW amplitude is negligible [37]. P1 and P1’, P2 and P2’, and P3 and P3’ are equidistant from the SAW beam path, and are 650 and 1250 μm above the IDTs and 650 μm below the IDTs, respectively. This arrangement allows

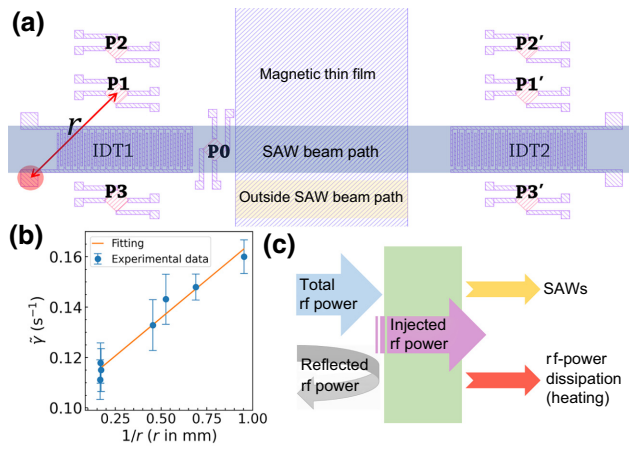


FIG. 4. (a) Layout of the SAW device showing seven thermometer positions: P0, located within the SAW beam path, and P1 (P1'), P2 (P2'), and P3 (P3') located outside the SAW beam path, at different distances from IDT1 (IDT2). Domain-wall velocity is also measured outside the SAW beam path (labeled as “outside SAW beam path”) to confirm the magnetoelastic coupling effect on domain-wall motion. (b) $\tilde{\gamma}$ against $1/r$ in the presence of a traveling SAW launched from IDT1, with a frequency of 48 MHz and power of 21 dBm. r is defined as the distance from the rf bond pad (red circle) to the center of the thermometer. The solid line represents the linear fitting of $\tilde{\gamma}$ against $1/r$. (c) The rf-power breakdown.

us to determine whether heating is from the SAW itself (acoustothermal heating) or from rf-power dissipation. We consider two possible sources of heating: acoustothermal heating and rf-power dissipation. If the heating is due to the acoustothermal effect, the highest $\tilde{\gamma}$ value would be expected within the beam path, while if it is due to rf-power dissipation, the highest $\tilde{\gamma}$ value would occur at the thermometer closest to the rf bond pad.

In Fig. 4(b), the heating rate $\tilde{\gamma}$ obtained at various locations in response to the traveling SAWs generated from IDT1 are presented. It is observed that the heating rate at P0 is $0.130 \pm 0.010 \text{ s}^{-1}$, which is lower than the values measured at P1 ($0.148 \pm 0.005 \text{ s}^{-1}$) and P3 ($0.160 \pm 0.007 \text{ s}^{-1}$). This indicates that P1 and P3 are located closer to the heating source than P0. Furthermore, under the same conditions, the heating rates at P1' ($0.118 \pm 0.008 \text{ s}^{-1}$) and P3' ($0.115 \pm 0.008 \text{ s}^{-1}$) are lower than those measured at P1 and P3, respectively, suggesting that the heating source is situated close to IDT1, where the rf power is applied. The origin of this heating is therefore likely to be power dissipated at the IDT in the radio frequency to the SAW transduction process. Notably, a good linear relationship is observed for $\tilde{\gamma}$ versus the reciprocal of the distance between the bond pad [where the rf power is applied, red circle shown in Fig. 4(a)] and the center of the thermometer. Besides, the heating rate $\tilde{\gamma}$ is much higher at P1 and P3 than at P0, where SAWs are excited. On the basis of these results, we conclude that the heating observed in

our SAW-magnetic thin film system is predominantly from rf-power dissipation rather than from the acoustothermal heating effect introduced by SAW itself.

Figure 4(c) presents a breakdown of the rf-power flow in our device. When rf signals are applied to the IDTs, a portion of the power is reflected back to the source, while the rest is injected into the IDTs. The proportion of the rf power converted accordingly is influenced by several factors: (i) the reflection at the connection between the SMA cable and bond pads, (ii) the reflection at the bond pads to IDTs, and (iii) the reflection coefficient of the IDTs (S_{11} or S_{22}), which are all sensitive to the radio frequency. Among these factors, the greatest reflection appears from the reflection coefficient of the IDTs, given that no impedance matching is used. The injected power is calculated by subtraction of the reflected rf power from the total rf power. A portion of the injected power is converted into surface acoustic waves, which is dependent on the electromechanical coefficient of the lithium niobate, while the remaining injected power is dissipated in the form of heating. Therefore, the S parameters and other reflections influence both the rf heating and the SAW amplitude, with a greater heating effect also corresponding to a higher SAW amplitude.

We then examine the relationship between temperature and DW velocity. Figure 5(a) shows the DW velocity within the SAW beam path against the applied magnetic field. The DW velocity is firstly measured at room temperature (approximately 19°C). As the field increases from 47 to 65 Oe, the DW velocity increases from $3 \pm 2 \text{ }\mu\text{m/s}$ to $33 \pm 3 \text{ }\mu\text{m/s}$. As depicted in Fig. 5(b), a plot of $\ln v$ against $H^{-1/4}$ shows the linear dependence as in Eq. (1). This indicates that the DW motion is in the creep regime, where thermal energy enables DWs to overcome the pinning barriers. DW creep motion can therefore be enhanced by increasing the temperature [Eq. (1)]. We study the temperature dependence of the DW velocity by heating our device by 10, 20, and 30 K using a Peltier device. As shown in Fig. 5(a), DW motion is significantly enhanced as temperature increases. For instance, under a field of 65 Oe, DW velocity increases from $33 \pm 3 \text{ }\mu\text{m/s}$ at room temperature to $650 \pm 30 \text{ }\mu\text{m/s}$ when the temperature is increased by 30 K. The DW motion remains in the creep regime as $\ln v$ shows a linear dependence on $H^{-1/4}$ [see Fig. 5(b)].

DW velocity is measured in the presence of SAWs at the same position within the SAW beam path. The frequency and power of both standing and traveling SAWs are set at 48 MHz and 21 dBm, respectively. DW motion is found to be enhanced in the presence of both types of SAWs [see Fig. 5(a)]. With the application of traveling SAWs, DW velocity is $116 \pm 3 \text{ }\mu\text{m/s}$ at 65 Oe, representing an approximately 2.5-fold increase compared with that measured at room temperature. However, even greater enhancement of DW motion can be observed in the presence of standing SAWs, with a velocity of $418 \pm 8 \text{ }\mu\text{m/s}$,

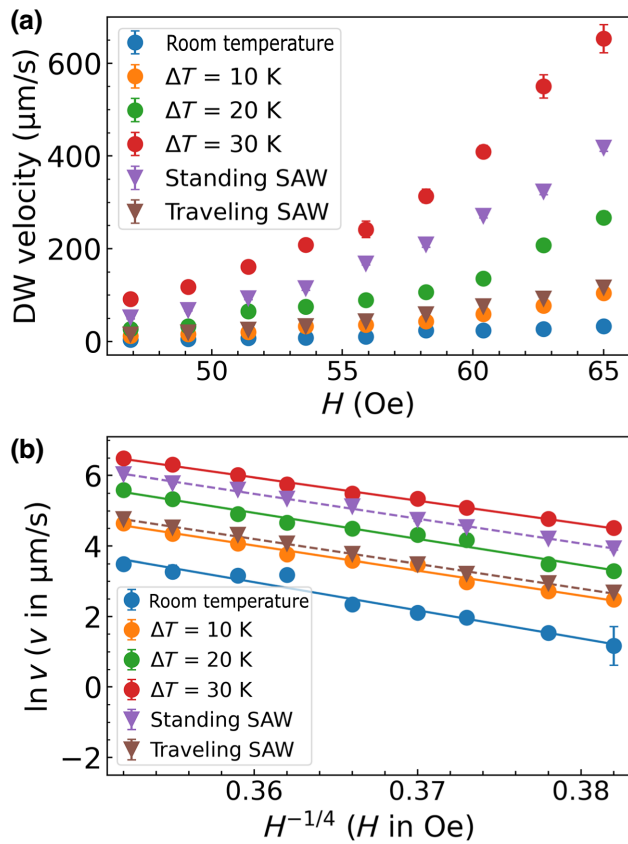


FIG. 5. (a) DW velocity as a function of the applied field (H). (b) Natural logarithm of DW velocity (v) as a function of $H^{-1/4}$. DW velocity is measured at different temperatures from room temperature up to $\Delta T = 30$ K without SAWs (circles) and in the presence of standing SAWs and traveling SAWs at a center frequency of 48 MHz and rf power of 21 dBm without additional heating (triangles). The solid and dashed lines are linear fittings of the DW-velocity experimental data at different temperatures and in the presence of the SAWs, respectively.

which is an increase of approximately 11.7-fold from the room-temperature measurement. DW motion is still thus within the creep regime in the presence of both traveling and standing SAWs over the measured field range [see Fig. 5(b)]. The Kerr-microscope images of the DW profile under different experimental conditions are presented in Fig. 6.

The DWs are nucleated at the left-hand side [indicated as “DW initial position” in Fig. 6(a)]. The DWs move toward the right-hand side [indicated as “DW final position” in Fig. 6(a)] driven by a magnetic field with or without SAWs. The DW exhibits a mostly smooth profile when subjected to a magnetic field of 65 Oe, as shown in Fig. 6(a). Increasing the temperature by 10 K [Fig. 6(b)] or introducing standing SAWs [Fig. 6(c)] and traveling SAWs [Fig. 6(d)] does not cause any significant changes in the DW profile.

The DW-motion enhancement we observe in the presence of SAWs is caused by a combination of both

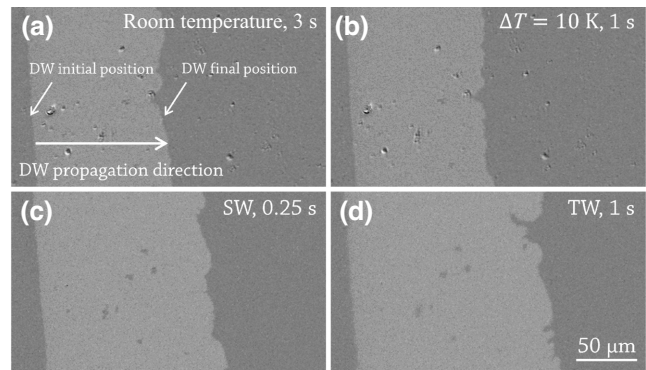


FIG. 6. Domain-wall profile under different experimental conditions imaged with a Kerr microscope. (a) Magnetic field applied at room temperature for 3 s, (b) magnetic field applied with a temperature increase of 10 K for 1 s, (c) standing SAWs with magnetic field applied for 0.25 s, and (d) traveling SAWs with magnetic field applied for 1 s. The magnetic field strength used is 65 Oe, and the frequency and power of the SAWs are 48 MHz and 21 dBm, respectively. The arrow in (a) indicates the direction of the domain-wall propagation.

the magnetoelastic coupling effect and the heating effect induced by rf-power dissipation, as the thermometer experiences a temperature increase of approximately 10 K at 48 MHz (as shown in Table I). As shown in Fig. 5(a), the DW-velocity curve with a 10-K temperature increase is similar to the traveling-SAW-assisted-DW-velocity curve. However, the DW-motion enhancement observed with standing SAWs is much greater than that achieved by our increasing the temperature by 10 K alone. Our results suggest that the heating plays the major role in promoting DW motion in the presence of traveling SAWs, whereas, the magnetoelastic coupling effect is the primary factor for significant DW motion with the application of standing SAWs.

Our study underlines the fact that heating is not negligible in SAW thin-film systems, especially with higher-power SAWs. DW-velocity measurements are performed at a location 100 μm from the beam path [labeled as “outside SAW beam path” in Fig. 4(a)]. This location is chosen because the heating effect is still present but to a lesser degree and the SAW amplitude is negligible in that area [25,37]. With an applied magnetic field of 65 Oe, the DW velocity increases from 33 ± 2 $\mu\text{m/s}$ at room temperature to 75 ± 3 $\mu\text{m/s}$ and 78 ± 4 $\mu\text{m/s}$ on application of standing and traveling SAWs, respectively. This DW-velocity increase outside the SAW beam path confirms the role of heating in enhancing DW motion.

Strain can modify the magnetic anisotropy of thin films through the magnetoelastic coupling effect [10,38–40]. The resulting changes in magnetic anisotropy create a dynamic energy landscape that reduces the energy requirement for DW motion. Specifically, the dynamic strain waves associated with the SAWs cause the magnetic

anisotropy to periodically change, increasing the possibility of DW depinning from pinning sites and facilitating faster DW motion.

IV. CONCLUSION

In conclusion, we explore the impact of both heating and SAWs in a SAW-driven magnetic film system, measuring the impact of both heating and SAWs on domain-wall velocity. Heating of approximately 10 K is observed within the SAW beam path when rf power is applied. DW velocity is measured at various temperatures both with and without SAWs. The DW velocity increases from $33 \pm 3 \mu\text{m/s}$ to $650 \pm 30 \mu\text{m/s}$ as the temperature rises from 19°C to 49°C at 65 Oe. The DW-velocity increase caused by traveling SAWs ($116 \pm 3 \mu\text{m/s}$) is slightly greater than that resulting from a 10-K temperature increase ($104 \pm 8 \mu\text{m/s}$), suggesting that heating plays the major role in promoting DW motion. On the other hand, DW motion is significantly enhanced in the presence of standing SAWs ($418 \pm 8 \mu\text{m/s}$) due to the dominant effect of magnetoelastic coupling. Our study underscores the importance of considering heating in SAW devices, especially with high rf power, and presents a straightforward way of measuring heating in SAW devices.

The data that support the findings of this study are available in the University of Leeds repository at <https://doi.org/10.5518/1336>.

ACKNOWLEDGMENTS

The authors gratefully acknowledge funding from the European Union's Horizon 2020 research and innovation program under the Marie Skłodowska-Curie Grant Agreement No. 860060, "Magnetism and the effect of Electric Field" (MagnEFi). J.S gratefully acknowledges productive discussions with Rutvij Bhavsar regarding the heating model, the assistance from Dr Nathan Satchell on low-temperature measurements, and thanks Prateek Dash for developing the code for the analysis of DW velocity. J.E.C. gratefully acknowledges funding from EPSRC (EP/V004743/1, EP/V047914/1, and EP/W028921/1). R.G.H. acknowledges the support of an EPSRC Doctoral Training Partnerships.

The authors have no conflicts to disclose.

[1] F. Cayssol, D. Ravelosona, C. Chappert, J. Ferré, and J. Jamet, Domain Wall Creep in Magnetic Wires, *Phys. Rev. Lett.* **92**, 107202 (2004).
 [2] L. Herrera Diez, F. García-Sánchez, J.-P. Adam, T. Devolder, S. Eimer, M. El Hadri, A. Lamperti, R. Manton, B. Ocker, and D. Ravelosona, Controlling magnetic domain wall motion in the creep regime in He^+ -irradiated CoFeB/MgO films with perpendicular anisotropy, *Appl. Phys. Lett.* **107**, 032401 (2015).

[3] D. Kumar, T. Jin, R. Sbiaa, M. Kläui, S. Bedanta, S. Fukami, D. Ravelosona, S.-H. Yang, X. Liu, and S. Pira-manayagam, Domain wall memory: Physics, materials, and devices, *Phys. Rep.* **958**, 1 (2022).
 [4] I. M. Miron, T. Moore, H. Szabolcs, L. D. Buda-Prejbeanu, S. Auffret, B. Rodmacq, S. Pizzini, J. Vogel, M. Bonfim, A. Schuhl, *et al.*, Fast current-induced domain-wall motion controlled by the Rashba effect, *Nat. Mater.* **10**, 419 (2011).
 [5] S. S. Parkin, M. Hayashi, and L. Thomas, Magnetic domain-wall racetrack memory, *Science* **320**, 190 (2008).
 [6] K.-S. Ryu, L. Thomas, S.-H. Yang, and S. Parkin, Chiral spin torque at magnetic domain walls, *Nat. Nanotechnol.* **8**, 527 (2013).
 [7] A. Schellekens, A. Van den Brink, J. Franken, H. Swagten, and B. Koopmans, Electric-field control of domain wall motion in perpendicularly magnetized materials, *Nat. Commun.* **3**, 1 (2012).
 [8] P. Chauve, T. Giamarchi, and P. Le Doussal, Creep and depinning in disordered media, *Phys. Rev. B* **62**, 6241 (2000).
 [9] P. Metaxas, J. Jamet, A. Mougin, M. Cormier, J. Ferré, V. Baltz, B. Rodmacq, B. Dieny, and R. Stamps, Creep and Flow regimes of Magnetic Domain-Wall Motion in Ultrathin Pt/Co/Pt Films with Perpendicular Anisotropy, *Phys. Rev. Lett.* **99**, 217208 (2007).
 [10] P. Shepley, A. Rushforth, M. Wang, G. Burnell, and T. Moore, Modification of perpendicular magnetic anisotropy and domain wall velocity in Pt/Co/Pt by voltage-induced strain, *Sci. Rep.* **5**, 1 (2015).
 [11] E. E. Ferrero, S. Bustingorry, A. B. Kolton, and A. Rosso, Numerical approaches on driven elastic interfaces in random media, *C. R. Phys.* **14**, 641 (2013).
 [12] W.-G. Yang and H. Schmidt, Acoustic control of magnetism toward energy-efficient applications, *Appl. Phys. Rev.* **8**, 021304 (2021).
 [13] I. Camara, J.-Y. Duquesne, A. Lemaître, C. Gourdon, and L. Thevenard, Field-Free Magnetization Switching by an Acoustic Wave, *Phys. Rev. Appl.* **11**, 014045 (2019).
 [14] L. Thevenard, I. S. Camara, S. Majrab, M. Bernard, P. Rovillain, A. Lemaître, C. Gourdon, and J.-Y. Duquesne, Precessional magnetization switching by a surface acoustic wave, *Phys. Rev. B* **93**, 134430 (2016).
 [15] L. Thevenard, J.-Y. Duquesne, E. Peronne, H. J. Von Bardeleben, H. Jaffres, S. Ruttala, J.-M. George, A. Lemaître, and C. Gourdon, Irreversible magnetization switching using surface acoustic waves, *Phys. Rev. B* **87**, 144402 (2013).
 [16] W. Li, B. Buford, A. Jander, and P. Dhagat, Acoustically assisted magnetic recording: A new paradigm in magnetic data storage, *IEEE Trans. Magn.* **50**, 37 (2014).
 [17] J. Shuai, M. Ali, L. Lopez-Diaz, J. E. Cunningham, and T. A. Moore, Local anisotropy control of Pt/Co/Ir thin film with perpendicular magnetic anisotropy by surface acoustic waves, *Appl. Phys. Lett.* **120**, 252402 (2022).
 [18] A. Adhikari and S. Adenwalla, Surface acoustic waves increase magnetic domain wall velocity, *AIP Adv.* **11**, 015234 (2021).
 [19] Y. Cao, X. Bian, Z. Yan, L. Xi, N. Lei, L. Qiao, M. Si, J. Cao, D. Yang, and D. Xue, Surface acoustic wave-assisted

- spin-orbit torque switching of the Pt/Co/Ta heterostructure, *Appl. Phys. Lett.* **119**, 012401 (2021).
- [20] W. Edrington, U. Singh, M. A. Dominguez, J. R. Alexander, R. Nepal, and S. Adenwalla, Saw assisted domain wall motion in Co/Pt multilayers, *Appl. Phys. Lett.* **112**, 052402 (2018).
- [21] E. Vilkov, O. Byshevski-Konopko, P. Stremoukhov, A. Safin, M. Logunov, D. Kalyabin, S. Nikitov, and A. Kirilyuk, Magnetic domain wall motion driven by an acoustic wave, *Ultrasonics* **119**, 106588 (2022).
- [22] Y. Wei, X. Li, R. Gao, H. Wu, X. Wang, Z. Zeng, J. Wang, and Q. Liu, Surface acoustic wave assisted domain wall motion in [Co/Pd]₂/Pd(t)/Py multilayers, *J. Magn. Magn. Mater.* **502**, 166546 (2020).
- [23] J. Dean, M. Bryan, J. Cooper, A. Virbule, J. Cunningham, and T. Hayward, A sound idea: Manipulating domain walls in magnetic nanowires using surface acoustic waves, *Appl. Phys. Lett.* **107**, 142405 (2015).
- [24] A. Adhikari, E. Gilroy, T. Hayward, and S. Adenwalla, Surface acoustic wave assisted depinning of magnetic domain walls, *J. Phys.: Condens. Matter* **33**, 31LT01 (2021).
- [25] J. Han, F. Yang, H. Hu, Q. Huang, Y. Lei, and M. Li, Thermal control design and packaging for surface acoustic wave devices in acoustofluidics, *IEEE Trans. Ultrason. Ferroelectr. Freq. Control* **69**, 386 (2021).
- [26] R. J. Shilton, V. Mattoli, M. Travaglini, M. Agostini, A. Desii, F. Beltram, and M. Cecchini, Rapid and controllable digital microfluidic heating by surface acoustic waves, *Adv. Funct. Mater.* **25**, 5895 (2015).
- [27] P. Utko, P. E. Lindelof, and K. Gloos, Heating in single-electron pumps driven by surface acoustic waves, *Appl. Phys. Lett.* **88**, 202113 (2006).
- [28] T. Zheng, C. Wang, Q. Hu, and S. Wei, The role of electric field in microfluidic heating induced by standing surface acoustic waves, *Appl. Phys. Lett.* **112**, 233702 (2018).
- [29] P. K. Das, A. D. Snider, and V. R. Bhethanabotla, Acoustothermal heating in surface acoustic wave driven microchannel flow, *Phys. Fluids* **31**, 106106 (2019).
- [30] B. H. Ha, K. S. Lee, G. Destgeer, J. Park, J. S. Choung, J. H. Jung, J. H. Shin, and H. J. Sung, Acoustothermal heating of polydimethylsiloxane microfluidic system, *Sci. Rep.* **5**, 1 (2015).
- [31] J. Kondoh, N. Shimizu, Y. Matsui, M. Sugimoto, and S. Shiokawa, Development of temperature-control system for liquid droplet using surface acoustic wave devices, *Sens. Actuators A: Phys.* **149**, 292 (2009).
- [32] K. Kulkarni, J. Friend, L. Yeo, and P. Perlmutter, Surface acoustic waves as an energy source for drop scale synthetic chemistry, *Lab Chip* **9**, 754 (2009).
- [33] J. Park, B. H. Ha, G. Destgeer, J. H. Jung, and H. J. Sung, An acoustothermal heater for paper microfluidics towards point-of-care glucose detection, *Phys. Procedia* **70**, 46 (2015).
- [34] Y. Wang, Q. Zhang, R. Tao, D. Chen, J. Xie, H. Torun, L. E. Dodd, J. Luo, C. Fu, J. Vernon, *et al.*, A rapid and controllable acoustothermal microheater using thin film surface acoustic waves, *Sens. Actuators A: Phys.* **318**, 112508 (2021).
- [35] R. Weser, Z. Deng, V. V. Kondalkar, A. N. Darinskii, C. Cierpka, H. Schmidt, and J. König, Three-dimensional heating and patterning dynamics of particles in microscale acoustic tweezers, *Lab Chip* **22**, 2886 (2022).
- [36] See Supplemental Material <http://link.aps.org/supplemental/10.1103/PhysRevApplied.20.014002> for the rf circuit used to generate SAWs, the determination of the temperature of the thermometer and the DW velocity, and the temperature changes of the Pt thermometer over a wider frequency range.
- [37] A. Winkler, S. Harazim, D. Collins, R. Brünig, H. Schmidt, and S. Menzel, Compact saw aerosol generator, *Biomed. Microdevices* **19**, 1 (2017).
- [38] Y. Ba, S. Zhuang, Y. Zhang, Y. Wang, Y. Gao, H. Zhou, M. Chen, W. Sun, Q. Liu, G. Chai, *et al.*, Electric-field control of skyrmions in multiferroic heterostructure via magnetoelectric coupling, *Nat. Commun.* **12**, 1 (2021).
- [39] D. Bhattacharya, S. A. Razavi, H. Wu, B. Dai, K. L. Wang, and J. Atulasimha, Creation and annihilation of non-volatile fixed magnetic skyrmions using voltage control of magnetic anisotropy, *Nat. Electron.* **3**, 539 (2020).
- [40] C. Feng, F. Meng, Y. Wang, J. Jiang, N. Mehmood, Y. Cao, X. Lv, F. Yang, L. Wang, Y. Zhao, *et al.*, Field-free manipulation of skyrmion creation and annihilation by tunable strain engineering, *Adv. Funct. Mater.* **31**, 2008715 (2021).